Three-dimensional instability and state selection in an oscillatory axisymmetric swirling flow

H. M. Blackburn[a)]
CSIRO Manufacturing and Infrastructure Technology, P.O. Box 56, Highett 3190, Australia

(Received 5 June 2002; accepted 5 August 2002; published 3 October 2002)

Previous studies of the flow created inside a cylindrical cavity (radius R, height H) of fluid by a single rotating end wall have shown that over a range of cylinder aspect ratios $1.6 \lesssim H/R \lesssim 2.8$, the first unsteady flows to bifurcate with increasing Reynolds number retain axisymmetry, and subsequent bifurcations break axisymmetry to give solutions with modulated rotating wave (MRW) states. The underlying axisymmetric components of these MRW flows are nearly indistinguishable from corresponding axisymmetric flows at the same Reynolds numbers. Of the three solution branches so far identified for this flow at $H/R=2.5$, only one both supports MRWs and has a simple limit-cycle underlying axisymmetric flow. Here, we carry out three-dimensional Floquet stability analysis of this branch of axisymmetric solutions and demonstrate that only a subset of the linearly unstable MRWs are observed asymptotically at large times for full Navier–Stokes solutions. Stability analysis of the time-average axisymmetric flow shows rotating wave (RW) instabilities that are in many ways similar to the MRW Floquet modes. The orientation of the vorticity of the RW and MRW structures implies that they are unlikely to originate as centrifugal instabilities, while simplified inviscid shear flow stability analysis of the time-average velocity profiles suggests instead that they arise as a result of inflectional instability of the swirling wall-jet flow contained by the cylindrical walls of the cavity. © *2002 American Institute of Physics.* [DOI: 10.1063/1.1509452]

I. INTRODUCTION

The flow produced inside a cylindrical cavity by a single steadily rotating end wall is a prototypical swirling flow with interesting dynamical properties. The system possesses just a single geometrical symmetry (rotation about the axis, the $SO(2)$ symmetry) and has two control parameters, the cylinder aspect ratio $\Lambda=H/R$ and the Reynolds number $\mathrm{Re}=\Omega R^2/\nu$, where H and R are the height and radius of the cylinder, Ω is the angular velocity of the rotating end wall, and ν is the kinematic viscosity of the fluid. The Ekman layer produced by rotation of the end wall is diverted along the stationary cylindrical walls to form a swirling wall-jet like flow which is turned radially inwards, toward the axis, by the stationary end wall, before swirling back along the axis. A schematic of the flow configuration is presented in Fig. 1.

Much of the early interest in this flow followed the discovery[1] that vortex breakdowns (regions of reversed axial flow) could occur on the axis of the cavity. Subsequently the regimes for onset of vortex breakdowns (up to three regions along the axis) were mapped in (Λ, Re) control space[2]—in that work, Reynolds numbers for onset of breakdowns were found to be low enough that the flows remained steady in time. The steady flow illustrated in Fig. 1 (for $\Lambda=2.5$) has a double breakdown. It was also found that $\Lambda>1.2$ is required for breakdowns to occur.

At moderate aspect ratios, flows become unsteady with further increase in Reynolds number above that required to produce vortex breakdown,[2–4] but the flows retain axisymmetry at the onset of unsteadiness. It is to be expected, however, that unsteady states with rotating waves (RWs) should also occur, as these are ubiquitous features of $SO(2)$ swirling flows.[5,6] The issue of which kind of unsteadiness bifurcates first as Reynolds numbers are increased at arbitrary Λ was resolved in a numerical study[7] of general three-dimensional perturbations to steady basic states. (The steady solutions are also referred to as the ''basic states'' for these flows, as they share the same ''basic'' symmetries, $SO(2)$ and time-translation, as the governing equations and boundary conditions.) At intermediate aspect ratios, $1.6<\Lambda<2.8$, the onset of unsteadiness occurs through a supercritical Hopf bifurcation to periodic axisymmetric flows. For $\Lambda<1.6$, the Hopf bifurcation is to a RW with wave number $k=2$, while for $\Lambda>2.8$, it is to a RW with $k=4$ (and subsequently other wave numbers as Λ or Re are further increased).[7,8] At the critical values $\Lambda=1.6$ and 2.8, both types of Hopf bifurcations are possible, and the dynamics of the codimension-2 double Hopf bifurcation behavior at $\Lambda=1.6$ has been investigated.[9]

The behavior subsequent to the initial Hopf bifurcation to periodic axisymmetric flow at intermediate aspect ratios (and in particular, $\Lambda=2.5$) has been the subject of experiments,[10] axisymmetric stability analysis of the equivalent steady flows,[11] and both two-dimensional and three-dimensional direct numerical simulation (DNS) studies.[10,12,13] The most fundamental conclusion derived from the experiments and simulations is that the behavior is dominated by the axisymmetric component of the flow, even when three-dimensional RWs are present. This conclusion is supported by the observations that typically of order 99% of

a)Electronic mail: hugh.blackburn@csiro.au

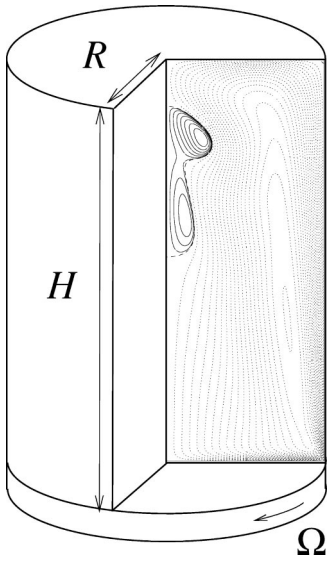

FIG. 1. Schematic of the flow configuration, a cylindrical container of fluid with a single rotating end wall, showing inset contours of streamfunction for a double vortex-breakdown flow.

the flow kinetic energy is contained in the axisymmetric (wave number $k=0$) component of the flow after it becomes three-dimensional,[12] and that the major solution branches and the frequency content of the axisymmetric component of the associated flows are reproduced quite well by axisymmetric simulations,[10,13] as illustrated in Fig. 2.

Referring to Fig. 2, the experiments and axisymmetric simulations show similar behavior in terms of number of solution branches, fundamental oscillation periods, and Re extent of branches (the Re extents predicted by three-dimensional DNS are in better agreement with the experiments[13]). The onset of unsteady behavior occurs through a supercritical Hopf bifurcation near $\mathrm{Re}=2707$[7,11,13] to axisymmetric periodic flows that are stable to three-dimensional perturbations; this is the *A* solution branch, for which the period $\Omega T \approx 36$. Starting near $\mathrm{Re}=3500$, another

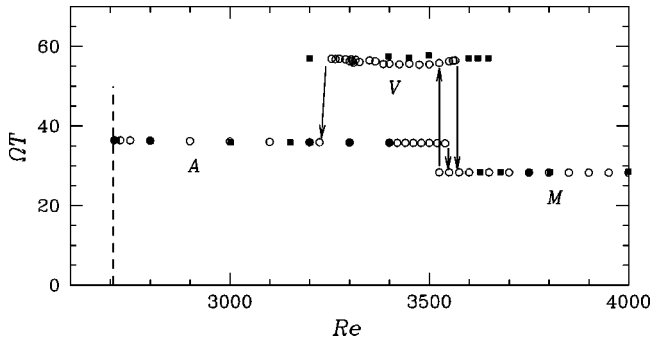

FIG. 2. Solution branches of unsteady flows at $\Lambda=2.5$. Fundamental oscillation periods ΩT for axisymmetric simulations (○), as a function of Reynolds number, with transitions between different solution branches indicated (Ref. 13). Also shown are experimentally measured values—Ref. 10 (■). Solutions on the *V* branch are quasiperiodic, with additional very-low-frequency modulations, while the *A* and *M* branches have periodic solutions. The dashed line at $\mathrm{Re}=2707$ indicates the Reynolds number for the onset of unsteadiness. Solutions of the *V* and *M* branches support rotating wave instabilities, while those of *A* retain axisymmetry.

solution branch can be observed; the *M* solution branch, which in the axisymmetric restriction has periodic solutions with $\Omega T \approx 28.3$ and which extends out to higher Reynolds number (at least $\mathrm{Re}=4300$, according to DNS results so far obtained[13]). Solutions of this branch are unstable to RWs, the energies of which are modulated in time by the underlying axisymmetric behavior, leading to so-called modulated rotating waves (MRWs). Overlapping the *A* and *M* solution branches in Re extent is the *V* solution branch, with $\Omega T \approx 57$, but with in addition a much longer period very low frequency (VLF) modulation. Of the three, the dynamics of the *V* branch are the most complex, with solutions being unstable to RWs over some (but not all) of its extent, in addition to the VLF behavior, which exhibits a period-doubling cascade in the three-dimensional case.[13]

The relationship between the *A*, *M*, and *V* solution branches and the predictions of axisymmetric stability analysis[11] of the corresponding steady flows is interesting. The (*note*: axisymmetric) stability analysis predicts that as Reynolds numbers are increased, a succession of Hopf bifurcations to unsteady states occur—at $\Lambda=2.5$, the first three bifurcations take place at $\mathrm{Re}=2707$, 3040, and 3150. The predicted frequency of the bifurcated state and its onset Reynolds number unambiguously link the first Hopf bifurcation with the *A* solution branch. Likewise the predicted frequency associated with the third Hopf bifurcation links it to the *M* solution branch. It might therefore be expected that there would be a clear link between the states corresponding to the second Hopf bifurcation and the remaining, *V*, solution branch, although this seems not to be the case. The behavior on the *V* branch suggests that it may have mixed-mode characteristics, and it has been conjectured[13] that it results from interactions between various pairings of the first three Hopf-bifurcated states.

In the present investigation we seek to more fully understand the three-dimensional instabilities of the *M* solution branch; such a study is amenable to Floquet analysis[14] as the underlying axisymmetric state is periodic in time for $\mathrm{Re} \gtrsim 3600$. The *V* solution branch, on the other hand, is not amenable to this analysis as the underlying states are quasi-periodic.

We commence a review of the observed behavior for the *M* solution branch with the axisymmetric M_0 flows: as in previous work[13] a subscript denotes the azimuthal wave number of the first harmonic of any three-dimensional behavior, with index 0 denoting axisymmetric flows or flows that are restricted to axisymmetry. While the periodic behavior of the *A*-branch flows is associated with oscillatory pulsations of the axial vortex breakdown region, that of the *M* branch is associated with a traveling-perturbation behavior, with disturbances (including vortex breakdowns) propagating along the axis, outwards across the rotating end wall, along the stationary walls, then axially in a repetitive cycle.[4,11] This behavior is illustrated for the state at $\mathrm{Re}=4000$ by the phase-specific sectional streamlines (computed in the meridional semiplane) shown in Fig. 3. Also shown are the sectional streamlines for the time-average flow and those for the corresponding steady flow, which has a single small vortex breakdown.

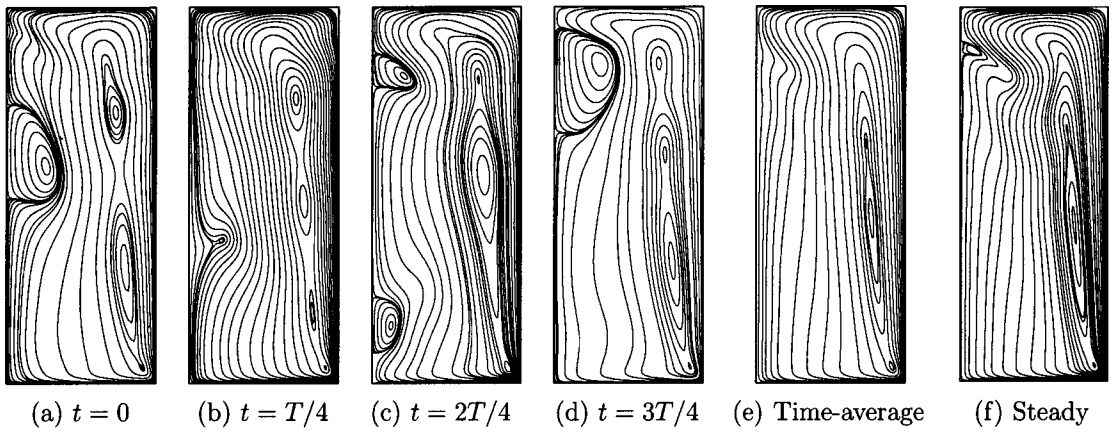

FIG. 3. Sectional streamlines in the meridional semiplane for axisymmetric flows at Re=4000: (a)–(d), instantaneous flows at four phases of the limit cycle and (e) time average for the periodic M_0 solution. Sectional streamlines of the basic state, i.e., the equivalent steady flow, are shown in (f). In each panel, the cylinder axis is on the left-hand side and the rotating end wall is at the bottom.

Turning now to review the symmetry-breaking solutions of the M branch, MRWs with fivefold or sixfold azimuthal periodicity have been observed as stable asymptotic states.[13] The flows evolve to a subspace of the full solution space, i.e., only Fourier modes that are harmonics of the lowest azimuthal periodicity survive asymptotically. In Fig. 4 the M_5 and M_6 states are illustrated for two solutions at Re=4000. The spatial structure of the two states is very similar, apart from the difference in wave number; the distributions of kinetic energy in the leading symmetry-breaking modes are similar in shape and location, and are associated with the swirling wall-jet flow clearly reflected in the contours of Fig. 4(c), rather than any near-axial features. Despite the temporal modulation in energy, the RWs precess around the cylindrical container at constant speed,[13] and in the same sense as the end wall rotation, with angular velocity $\omega = 0.132\ \Omega$.

II. OBJECTIVES AND APPROACH

The purpose of the present study is to provide three-dimensional stability analysis of the axisymmetric flows on the M solution branch, and to link the results to the MRW states so far observed. As the corresponding axisymmetric flows are periodic, the findings commence with Floquet stability analysis. It is found that the MRW states observed to be asymptotically stable in DNS studies correspond almost exactly to the most unstable Floquet modes, and a previously unobserved asymptotic state is documented: a MRW with a fourfold rotational symmetry, in addition to those with fivefold and sixfold symmetries.

Attention is then focused on three-dimensional stability of a time-average axisymmetric flow at Re=4000, which is found to support RWs over a comparable range of wave numbers, and with larger growth rates, to those predicted in the Floquet analysis. The mode shapes are in good agreement. The three-dimensional stability of the corresponding steady axisymmetric flow at Re=4000 is also examined. This flow marginally supports similar-shape RWs, with smaller growth rates and over a comparatively restricted band of wave numbers, but in addition is found to support two different modes, at wave numbers $k=1$ and $k=2$, that are not unstable for the periodic or time-average flows. Finally, stability characteristics of the velocity profiles for the

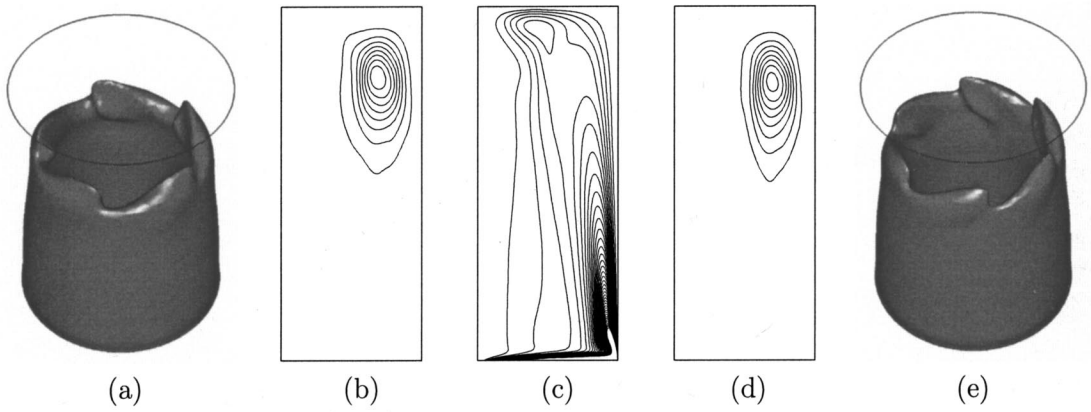

FIG. 4. MRW solutions on the M solution branch at Re=4000. Contours of kinetic energy in the time-average flow, $\langle \mathbf{u}\cdot\mathbf{u} \rangle/2$, are shown in (c), while (a), (b) and (d), (e), respectively, illustrate the M_5 and M_6 states: (b) and (d) show contours of time-average energy $\langle \hat{\mathbf{u}}_k \cdot \hat{\mathbf{u}}_k^* \rangle/2$ in the leading nonaxisymmetric mode ($k=5$ and $k=6$, respectively), and (a) and (e) show isosurfaces of instantaneous azimuthal velocity for the two states. In (a) and (e), the lower end wall rotates in a clockwise sense when viewed from above, as in Fig. 1.

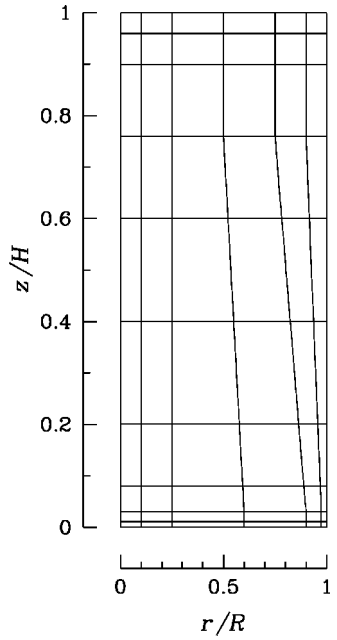

FIG. 5. Spectral element mesh used to discretize the meridional semiplane. Cylinder axis to the left-hand side, rotating end wall at bottom, 60 spectral elements.

time-average flow are examined using a Rayleigh-type analysis and it is concluded that the RW instability corresponds well to inviscid instability of the corresponding parallel wall-jet velocity profile.

III. NUMERICAL METHODS

The analytical techniques employed in this work are all associated with time-integration of the incompressible unsteady Navier–Stokes equations

$$\partial_t \mathbf{u} = -\mathbf{A}\mathbf{u} - \boldsymbol{\nabla} P + \nu \nabla^2 \mathbf{u},$$
$$\boldsymbol{\nabla}\cdot\mathbf{u} = 0, \tag{1}$$

in which $\mathbf{A}\mathbf{u}$ represents nonlinear advection terms—equivalently $\mathbf{u}\cdot\boldsymbol{\nabla}\mathbf{u}$, $\boldsymbol{\nabla}\cdot\mathbf{u}\mathbf{u}$, or $(\mathbf{u}\cdot\boldsymbol{\nabla}\mathbf{u}+\boldsymbol{\nabla}\cdot\mathbf{u}\mathbf{u})/2$—and $P = p/\rho$.

The numerical techniques used to integrate (1) are briefly outlined in Sec. III A. In the succeeding sections (Secs. III B–III E), the techniques used to obtain steady solutions and to perform stability analyses are described. These are based around time-integration of the Navier–Stokes equations and their linearized equivalents, and follow methods advanced by Tuckerman and Barkley (TB).[15] The modal structure and boundary conditions for perturbation velocities and pressures are discussed in Sec. III F. A resolution study for Floquet stability analysis is presented in Sec. III G.

A. Spatial discretization and time integration

Spatial discretization is carried out in a cylindrical coordinate system, using spectral elements in the meridional semiplane, coordinates (z,r), and Fourier expansions in azimuth, coordinate θ. The spectral element mesh employed is illustrated in Fig. 5. Time integration uses a mixed explicit–implicit time-stepping scheme,[16] and all simulations discussed here used second-order-time integration.

The method of solution of the discrete equations, the mesh, and the spatiotemporal resolution are all identical to those employed in previous studies.[12,13] The spectral element mesh has 60 elements, and tensor-products of seventh-order Gauss–Lobatto–Legendre (GLL) Lagrange shape functions are used within each element, providing a total of 3053 independent mesh points in the discretization of the meridional semiplane. To keep the overall account here reasonably brief, the reader is referred elsewhere[13] for a detailed description of the method and resolution studies as applied to DNS. A resolution study for Floquet stability analysis is supplied in Sec. III G.

The use of Fourier expansions in azimuth means that there is a one-to-one correspondence between wave number and Fourier mode index. This is convenient because, as noted previously, three-dimensional solutions in the full range of wave numbers are observed to evolve to asymptotic states that have P-fold azimuthal rotation symmetries, i.e., to invariant subspaces of the full set of Fourier modes—subspaces that leave the solution invariant after azimuthal rotations through $n2\pi/P$, $n\in\mathbb{I}$. By computing only with Fourier mode indices $k = nP$, solutions can be restricted to an invariant subspace, while retaining the option of projecting back to the full set of Fourier modes if required. This feature is exploited in the state selection studies of Sec. VI.

B. Operator notation

In order to condense the following treatment and to link it with that of TB, the incompressible Navier–Stokes equations (1) are first rewritten in symbolic form

$$\begin{aligned}\partial_t \mathbf{u} &= -\mathbf{A}\mathbf{u} - \boldsymbol{\nabla} P + \nu\nabla^2\mathbf{u} \\ &= -(\mathbf{I} - \boldsymbol{\nabla}\nabla^{-2}\boldsymbol{\nabla}\cdot)\mathbf{A}\mathbf{u} + \nu\nabla^2\mathbf{u} \\ &= \mathbf{N}\mathbf{u} + \mathbf{L}\mathbf{u},\end{aligned} \tag{2}$$

where the pressure is treated as the solution of a Poisson equation that has the divergence of the advection terms as forcing. The nonlinear operator $\mathbf{N}$ now contains contributions from both advection and pressure terms, while the linear operator $\mathbf{L}$ corresponds to viscous diffusion.

An operator that integrates (2) over an interval Δt is written as

$$\mathbf{u}(t+\Delta t) = \mathrm{NS}_{\Delta t}[\mathbf{u}(t)]. \tag{3}$$

For example, with mixed explicit–implicit Euler time-stepping this operator can be approximated using the above-introduced symbolic notation as

$$\mathrm{NS}_{\Delta t} \approx (\mathbf{I} - \Delta t\mathbf{L})^{-1}(\mathbf{I} + \Delta t\mathbf{N}), \tag{4}$$

however, the use of integration operators in what follows is not restricted to any particular approximate numerical implementation. For the results to be presented here, the discrete time integrations were implemented with the same second-order-time explicit–implicit scheme used in previous work.[12,13]

In stability analysis, we wish to study the evolution of a perturbation $\mathbf{u}'$ to a "base flow" $\mathbf{U}$, where $\mathbf{u} = \mathbf{U} + \mathbf{u}'$. Here,

the base flow **U** can be steady or T-periodic. The linearized equivalent of (2) for an infinitesimal perturbation $\mathbf{u}'$ can be written as

$$\partial_t \mathbf{u}' = \partial_U \mathbf{N}\mathbf{u}' + \mathbf{L}\mathbf{u}', \tag{5}$$

where $\partial_U \mathbf{N}+\mathbf{L}$ represents the linearization (Jacobian) of $\mathbf{N}+\mathbf{L}$ about the base flow **U**. We will use the notation $\mathrm{LNS}_{\Delta t}$ to denote an operator that integrates (5) over interval Δt, i.e., in analogy to (3)

$$\mathbf{u}'(t+\Delta t) = \mathrm{LNS}_{\Delta t}[\mathbf{u}'(t)]. \tag{6}$$

Since $\mathrm{LNS}_{\Delta t}$ is linear, it can also be written

$$\mathrm{LNS}_{\Delta t} = \exp[\Delta t(\partial_U \mathbf{N}+\mathbf{L})], \tag{7}$$

and interpreted as a matrix exponential operator.[17] For an Euler time step, the analog of the approximation (4) is

$$\mathrm{LNS}_{\Delta t} \approx (\mathbf{I}-\Delta t\mathbf{L})^{-1}(\mathbf{I}+\Delta t\partial_U \mathbf{N}). \tag{8}$$

In order to convert a time stepping code that provides a discrete approximation to $\mathrm{NS}_{\Delta t}$ to one that approximates $\mathrm{LNS}_{\Delta t}$, the main modification required is to replace the computation of **Au** with its linearized equivalent, e.g., $\mathbf{u}'\cdot\nabla\mathbf{U}+\mathbf{U}\cdot\nabla\mathbf{u}'$, although in addition the base flow **U** must be supplied as data.

C. Steady-state solution

Newton's method for solution of the steady incompressible Navier–Stokes equations

$$0 = \mathbf{N}\mathbf{U}+\mathbf{L}\mathbf{U} \tag{9}$$

is

$$(\partial_U \mathbf{N}+\mathbf{L})\mathbf{u}' = (\mathbf{N}+\mathbf{L})\mathbf{U}, \tag{10a}$$

$$\mathbf{U} \leftarrow \mathbf{U}-\mathbf{u}'. \tag{10b}$$

In practice, iterative methods must be used to invert (10a), but $\partial_U \mathbf{N}+\mathbf{L}$ is poorly conditioned and convergence can be slow or nonexistent. Stokes preconditioning[18] is used to improve convergence: both sides of (10a) are multiplied by operator $(\mathbf{I}-\Delta t\mathbf{L})^{-1}\Delta t$ and rearranged to produce

$$[(\mathbf{I}-\Delta t\mathbf{L})^{-1}(\mathbf{I}+\Delta t\partial_U \mathbf{N})-\mathbf{I}]\mathbf{u}' = [(\mathbf{I}-\Delta t\mathbf{L})^{-1}(\mathbf{I}+\Delta t\mathbf{N})-\mathbf{I}]\mathbf{U}. \tag{11}$$

Examining (4) and (8) we see that this is an approximation to

$$(\mathrm{LNS}_{\Delta t}-\mathbf{I})\mathbf{u}' = (\mathrm{NS}_{\Delta t}-\mathbf{I})\mathbf{U}, \tag{12}$$

and that the two sides of (12) are equivalent to increments in the velocity fields $\mathbf{u}'$ and **U** obtained by integrating either the linearized or full Navier–Stokes equations over interval Δt. Thus the iteration for steady solutions can exploit time-integration methods originally devised for the unsteady Navier–Stokes equations.

Typically the time interval Δt here is much longer than the time step used in the explicit–implicit time integration, which is restricted by CFL stability considerations. That is, the increments in (12) are approximated by discrete integration over many time steps.

Experience with the method suggests that the Bi-CGSTAB (bi-conjugate gradient stabilized) algorithm available in the Templates package[19] is somewhat superior in performance to the Bi-CGS (bi-conjugate gradient squared) algorithm used by TB to invert (12).

D. Stability analysis of time-invariant flows

In studying the stability of time-invariant base flows **U**, obtained either through solution of (9) or as the time-average of solutions to (2), we wish to find the leading, i.e., most unstable, eigenvalues $\gamma = \chi + i\psi$ of

$$(\partial_U \mathbf{N}+\mathbf{L})\mathbf{u}' = \gamma\mathbf{u}'; \tag{13}$$

those with largest real part χ. However, most available numerical methods obtain the dominant eigenvalues, i.e., those of largest magnitude. To overcome this difficulty, we study instead the exponential of $\partial_U \mathbf{N}+\mathbf{L}$ through solutions of (5),

$$\mathbf{u}'(t+\Delta t) = \exp[\Delta t(\partial_U \mathbf{N}+\mathbf{L})]\mathbf{u}'(t) \equiv \mathrm{LNS}_{\Delta t}[\mathbf{u}'(t)]. \tag{14}$$

The dominant eigenvalues of $\exp[\Delta t(\partial_U \mathbf{N}+\mathbf{L})]$ correspond to the leading eigenvalues of $\partial_U \mathbf{N}+\mathbf{L}$. If γ is an eigenvalue of $\partial_U \mathbf{N}+\mathbf{L}$, the corresponding eigenvalue of $\exp[\Delta t(\partial_U \mathbf{N}+\mathbf{L})]$ is $\Gamma = \exp(\gamma\Delta t)$, while the eigenvectors are the same. Provided that time steps are sufficiently small, the discrete integration of (5) over the (larger) interval Δt provides a good approximation to (14).

The Arnoldi method[20,15] is used to extract some number (typically 2–4) of the most dominant eigenpairs of $\mathrm{LNS}_{\Delta t}$. In practice, data to compute a greater number (K, typically 8–12) of eigenpairs are carried in the Krylov sequence $\mathbf{u}'_0$, $\mathrm{LNS}_{\Delta t}\mathbf{u}'_0$, $\mathrm{LNS}^2_{\Delta t}\mathbf{u}'_0$,…, $\mathrm{LNS}^{K-1}_{\Delta t}\mathbf{u}'_0$.

E. Floquet stability analysis of *T*-periodic flows

In Floquet stability analysis,[17,21] the base flow **U**, and through it the operator $\partial_U \mathbf{N}+\mathbf{L}$, is T-periodic. Perturbation solutions $\mathbf{u}'$ can be written as a sum of components $\tilde{\mathbf{u}}(t)\exp\sigma t$, where $\tilde{\mathbf{u}}(t)$ are the T-periodic Floquet eigenmodes of $\partial_U \mathbf{N}+\mathbf{L}$. Equivalent to the Floquet exponents σ are the Floquet multipliers μ, where $\mu = \exp\sigma T$. Both σ and μ are in general complex numbers, with nonzero imaginary components often indicating traveling-wave solutions in three-dimensional flows.

We now define the operator LNS_T which is equivalent to (6) with time interval $\Delta t = T$, the period of the base flow. Integration over one base flow period provides the mapping

$$\mathbf{u}'_{n+1} = \mathrm{LNS}_T(\mathbf{u}'_n), \tag{15}$$

where $\mathbf{u}'_n(t_0+nT)$ is the perturbation after n periods, starting at an arbitrary initial phase t_0 of the base flow. Operator LNS_T is equivalent to the linearized Poincaré map associated with the base flow. The eigenvalues of LNS_T are the same as the Floquet multipliers of $\partial_U \mathbf{N}+\mathbf{L}$, while its eigenvectors are the Floquet eigenmodes $\tilde{\mathbf{u}}(t)$ evaluated at phase t_0 of the base flow.

The same Krylov subspace iteration used to extract the dominant eigenvalues of $\mathrm{LNS}_{\Delta t}$ is used to obtain those of LNS_T. The only difference is that the data used to supply the T-periodic base flow are obtained through Fourier-series re-

construction from a limited number (typically 32) of time-slices obtained using (3) for the full Navier–Stokes equations.

F. Modal structure and boundary conditions for perturbation fields

We will be solving for the three-dimensional normal instability modes of an axisymmetric swirling base flow in a cylindrical coordinate geometry, with U, V and W, respectively, the axial, radial, and azimuthal components of $\mathbf{U}$. By adopting Fourier decomposition of the normal modes in azimuth the stability analysis can be pursued on a Fourier-mode basis, i.e., an independent stability analysis is carried out at each wave number k. This converts a three-dimensional analysis into a set of two-dimensional analyses. A modified version of the original Navier–Stokes solver is used to integrate (5) for the linearized evolution of a single perturbation Fourier mode.

In some applications[21] the base flow $\mathbf{U}$ is both two-dimensional, i.e., invariant in a third (homogeneous) spatial coordinate, and two-component, i.e., $\mathbf{U}\equiv(U,V,0)$ possesses only two nonzero components. The normal modes of a base flow that is both two-dimensional and two-component are invariant with respect to a change of sign in the homogeneous spatial coordinate. As a consequence, the generally complex perturbation Fourier mode

$$\hat{\mathbf{u}}'_k=(\hat{u}'_k.\Re+\mathrm{i}\hat{u}'_k.\Im,\hat{v}'_k.\Re+\mathrm{i}\hat{v}'_k.\Im,\hat{w}'_k.\Re+\mathrm{i}\hat{w}'_k.\Im),$$

$$\hat{p}'_k=\hat{p}'_k.\Re+\mathrm{i}\hat{p}'_k.\Im, \tag{16}$$

where $.\Re$ and $.\Im$ denote real and imaginary parts, respectively, and can be decomposed into two linearly independent but equivalent solutions

$$\hat{\mathbf{u}}'_{k,1}=(\hat{u}'_k.\Re,\hat{v}'_k.\Re,\mathrm{i}\hat{w}'_k.\Im),\quad \hat{p}'_{k,1}=\hat{p}'_k.\Re, \tag{17a}$$

$$\hat{\mathbf{u}}'_{k,2}=(\mathrm{i}\hat{u}'_k.\Im,\mathrm{i}\hat{v}'_k.\Im,\hat{w}'_k.\Re),\quad \hat{p}'_{k,2}=\mathrm{i}\hat{p}_k.\Im, \tag{17b}$$

only one of which need be computed—the other can be obtained through a phase shift of $\pi/2$ in the homogeneous spatial coordinate. In the problem under study here, $\mathbf{U}$ is again two-dimensional (axisymmetric) but now three-component (swirling), and the reflection symmetry of the normal modes is broken by the fact that the base flow has a nonzero azimuthal velocity, hence the fully complex form of (16) must be retained through the solution procedure.

On the solid walls of the cylindrical container, perturbation velocities are set to zero, and a ''high-order'' Neumann boundary condition[16] is applied to the perturbation pressure. On the cylinder axis ($r=0$), boundary conditions are wavenumber dependent:[13]

$$\begin{aligned}
&k=0:\ \partial_r\hat{u}'_0=\check{v}'_0=\check{w}'_0=\partial_r\hat{p}'_0=0;\\
&k=1:\ \hat{u}'_1=\check{v}'_1=\partial_r\check{w}'_1=\hat{p}'_1=0;\\
&k>1:\ \hat{u}'_k=\check{v}'_k=\check{w}'_k=\hat{p}'_k=0.
\end{aligned} \tag{18}$$

Here, the change of variables $\check{v}'_k=\hat{v}'_k+\mathrm{i}\hat{w}'_k$, $\check{w}'_k=\hat{v}'_k-\mathrm{i}\hat{w}'_k$ has been introduced in order to decouple viscous terms in the Fourier-transformed equivalents of (5).[22]

TABLE I. Results of a convergence study of Floquet analysis applied at Re=4000, $k=5$. Complex-conjugate Floquet multipliers are represented by a magnitude $|\mu|$ and angle $\angle\alpha$.

N_p	N_{tot}	ΩT	$\lvert\mu\rvert$	$\angle\alpha$ (rad)
4	1025	28.285	1.3596	±0.159 14
5	1581	28.260	1.4465	±0.147 25
6	2257	28.281	1.4384	±0.128 30
7	3053	28.282	1.4446	±0.127 74
8	3969	28.281	1.4443	±0.128 11
9	5005	28.281	1.4444	±0.128 20

G. Convergence results for Floquet analysis

Results of a convergence study for Floquet multipliers conducted at Re=4000, $k=5$, are presented in Table I. The order of the (one-dimensional) GLL shape functions used to form the tensor-product shape function basis within each element is represented by N_p, while the total number of degrees of freedom for the 60-element mesh shown in Fig. 5 is given by N_{tot}. In each case the time step $\Delta t=T/2048$, and 32 time slices of the T-periodic base flow were used to provide its Fourier series reconstruction. The results show that the magnitudes of the complex[23] Floquet multipliers, $|\mu|$, and their angles, $\angle\alpha$, have converged to three significant figures at $N_p=6$, but the higher resolution $N_p=7$ was selected to compute all the results presented here, in order to be consistent with the resolution used in previous DNS studies.[12,13]

IV. THE LOWER-RE LIMIT OF THE T-PERIODIC M_0 BRANCH

Before commencing three-dimensional stability analysis of flows of the M_0 branch, issues concerning the extent of the branch need to be clarified. As noted in Sec. I, the M solution branch is clearly associated with the third unsteady state to bifurcate from the steady basic state as Reynolds numbers are increased. That Hopf bifurcation occurs at Re =3150, but it can be concluded that the bifurcated states are unstable at these Reynolds numbers, as the branch cannot be followed down below Re~3550 (see Fig. 2). Near that point, solutions jump to the V branch, in both axisymmetric and three-dimensional DNS.[13] (Solutions of the V_0 branch always have one characteristic period near that of the M_0 branch $\Omega T\approx 28$ in addition to the $\Omega T\approx 57$ values seen in Fig. 2, and beating between the two frequencies accounts for the VLF at these Reynolds numbers.[13])

Further axisymmetric simulations conducted here as part of establishing the T-periodic base flows required for three-dimensional Floquet analysis of the M_0 solutions indicate that the M_0 branch solutions lose stability through an axisymmetric flip (period-doubling) bifurcation at Reynolds numbers in the range 3575–3600. This corresponds to a real, negative, Floquet multiplier leaving the unit circle in this Reynolds number range. At Re=3575, the growth rates are very small, and velocity component histories appear almost as period-doubled limit cycles, see Fig. 6. The growth rates increase as Reynolds number is decreased below 3575, but given sufficient integration time, all such period-doubled solutions asymptote to states on the V solution branch.

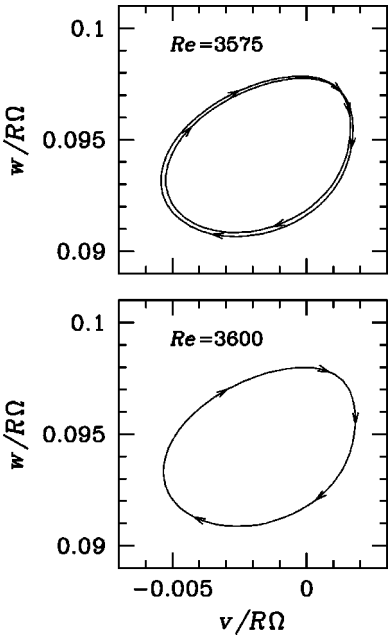

FIG. 6. At the lower Re limit of the M_0 branch, the periodic axisymmetric flow undergoes a flip bifurcation (period doubling) between Reynolds numbers 3575 and 3600. Loci of radial, v, and azimuthal, w, velocity components at ($z/H=4/5$, $r/R=2/3$).

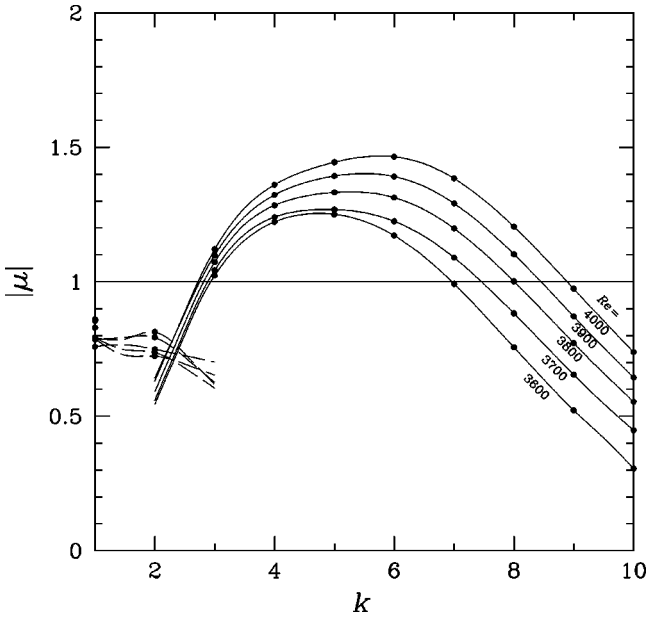

FIG. 7. Floquet multiplier magnitudes as functions of wave number k and Reynolds number Re.

The lower-Re limit of the three-dimensional Floquet analyses conducted in Sec. V is thus 3600. On the other hand, an upper-Re limit, if it exists, of the M solution branch has not been established, but it extends at least to Re $=4300$.[13] The analyses here are confined to Re$\leqslant$4000.

V. FLOQUET ANALYSIS RESULTS

Floquet multiplier magnitudes $|\mu|$ are shown as functions of wave number k in Fig. 7, for five Reynolds numbers commencing near the lower limit of the M_0 branch. The envelope of neutral-stability wave numbers is extracted to form the basis for Fig. 8, in which is also shown the approximate locus of the most-amplified wave numbers. The range of unstable wave numbers is broader than the wave numbers of asymptotic states from DNS, e.g., at Re$=$4000, wave numbers $k=3-8$ are all unstable, whereas only $P=5$ and $P=6$ asymptotic states were previously observed.[13] This point will be taken up in greater detail in Sec. VI, however it can be seen in Fig. 7 that $k=5$ and $k=6$ have the greatest amplification rates at Re$=$4000.

The fact that the envelope of neutral stability is open at the observed low-Re end of the M_0 branch reflects the fact that the solutions of the branch are unstable in an axisymmetric subspace, as well as to three-dimensional perturbations. Figure 7 suggests that M_0 can be stable to three-dimensional perturbations at lower Re, even though it is unstable to axisymmetric perturbations. New computational techniques enabling branch continuation of unstable limit cycle solutions are required before these issues can be fully resolved.

Before turning to examine the shape of the unstable Floquet modes, their speed of precession around the container will be examined, as this can be computed from the (complex) Floquet multipliers. It is known from the previous DNS studies that the RWs precess around the azimuth of the container with the same sense of rotation as the driven end wall. The angular velocity of precession is close to $\omega=0.132\ \Omega$ for MRWs of both the V and M solution branches. The dimensionless wave precession period, $T_w/T=2\pi/(0.132\ \Omega T)$, where T is the period of the axisymmetric base flow. For the observed extent of the M_0 branch, $\Omega T\approx 28.3$, giving $T_w/T\approx 1.68$.

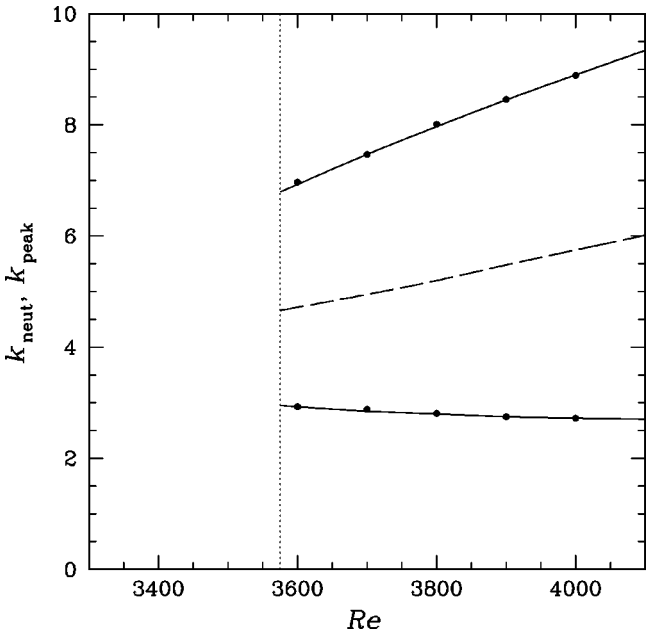

FIG. 8. Locations of neutral stability wave numbers (k_{neut}, solid lines) and approximate locations of most amplified wave numbers (k_{peak}, dashed line) as functions of Reynolds number Re. Dotted line indicates the approximate Reynolds number at which period doubling of the axisymmetric base flow occurs (Re$\approx$3575).

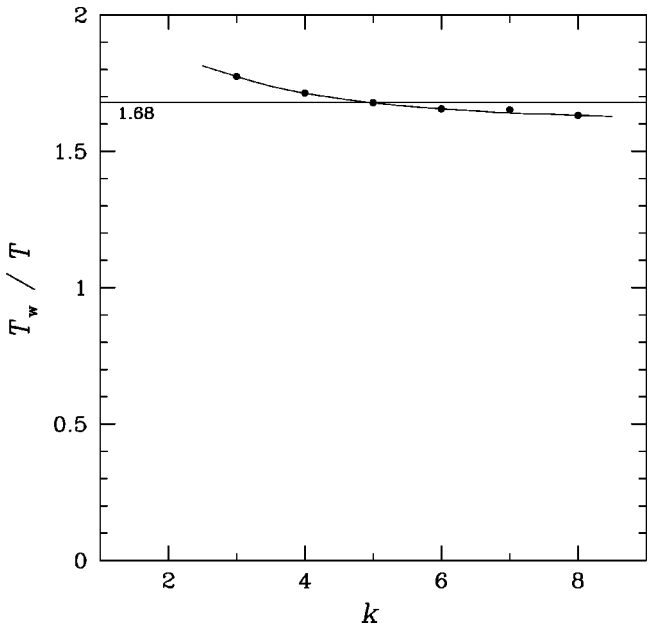

FIG. 9. Period of Floquet mode precession T_w normalized by the base flow period T as a function of wave number k for unstable Floquet modes at Re=4000. Horizontal line at value 1.68 shows result from direct simulation (Ref. 13).

The extraction of wave speed from the Floquet multipliers is complicated by aliasing. Consider a complex Floquet multiplier μ (one of a complex-conjugate pair) expressed in polar form as $(|\mu|,\angle\alpha)$ where at first α is taken not to be aliased into the range $[0,2\pi)$. If the passage of a RW through a single wave-number-k module takes a dimensionless period $T_w/(kT)$, the corresponding angular displacement of the wave in one base flow period T is

$$\alpha = \frac{2\pi kT}{T_w}, \tag{19}$$

however, we expect $kT/T_w > 1 \ \forall k \geqslant 1$ so that $\alpha \geqslant 2\pi$. Now consider aliasing: α will be aliased into the range $[0,2\pi)$, so that we have

$$\alpha + n2\pi = \frac{2\pi kT}{T_w}, \tag{20}$$

where $n \in \mathbb{I}$. Thus to compute a dimensionless wave precession period from a complex Floquet multiplier we must use

$$\frac{T_w}{T} = \frac{2\pi k}{\alpha + n2\pi}, \tag{21}$$

for arbitrary n and considering both multipliers of a complex-conjugate pair. The result of applying this analysis to the Floquet multipliers corresponding to unstable modes at Re=4000 is shown in Fig. 9. Only values of T_w/T closest to 1.68 are represented, for these form a smooth curve when connected. It can be seen that the RW periods predicted for the unstable Floquet modes are an excellent match for the value observed in DNS studies, especially near $k=5$ and $k=6$, from which the value $T_w/T=1.68$ was derived.

Now the shape of the unstable Floquet modes is examined; here again we concentrate on results for Re=4000. The distributions of kinetic energy $\langle \tilde{\mathbf{u}}'_k \cdot \tilde{\mathbf{u}}'^*_k \rangle/2$ in the meridional semiplane for one of the complex-conjugate pairs of leading Floquet modes at Re=4000 are shown in Fig. 10. By comparison with Fig. 2 it can be seen that the spatial distribution of energies in the Floquet modes is generally similar to that in the leading symmetry breaking modes in the DNS results, and the agreement is best for $k=5$ and $k=6$, which are the modes actually represented in Fig. 2. In most cases, perturbation energy is concentrated in regions remote from the axis, although the disturbances move closer to the top of the container and its axis as k drops. That the RW period should fall slightly as the wave number increases (Fig. 9) is consistent with the observation that as k increases, RWs move to larger radial locations while the time-average swirl velocity increases more rapidly than linearly with radius.

Isosurfaces of vorticity magnitude for the unstable Floquet modes at Re=4000 are shown in Fig. 11. The general locations of the isosurfaces agree with the regions of peak energy shown in Fig. 10 but additional important information is gained from the orientation of the structures. The fact that these perturbation vortices are not aligned with the direction

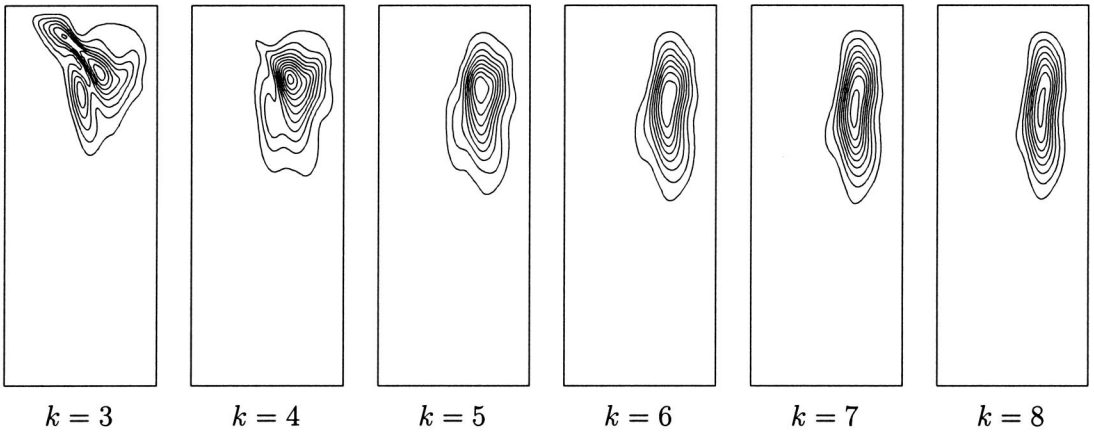

FIG. 10. Instantaneous contours of kinetic energy $\langle \tilde{\mathbf{u}}'_k \cdot \tilde{\mathbf{u}}'^*_k \rangle/2$ in the meridional semiplane for unstable Floquet modes at Re=4000 in wave numbers k as indicated. In each panel, the cylinder axis is to the left-hand side, rotating end wall at bottom.

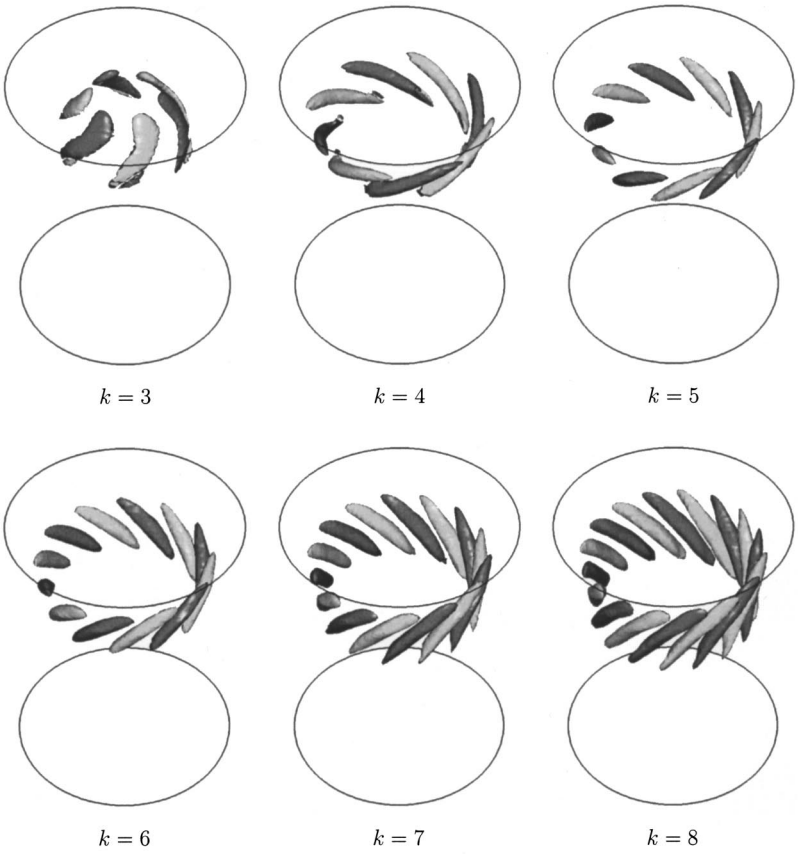

FIG. 11. Isosurfaces of vorticity magnitude for unstable Floquet modes at Re=4000 in wave numbers k as indicated. Isosurfaces are shaded according to the sign of the axial component of vorticity.

of time-mean flow streamlines, but are oriented with the time-mean streamlines crossing them at significant angles (typically near 45°) implies that the RWs do not result from centrifugal instability, as alignment is characteristic of centrifugal instabilities of the Taylor or Görtler types. Similarly, the fact that the perturbation vortices are counter-rotating shows that they do not result from crossflow instability.[24]

VI. STATE SELECTION

The fact that the spectrum of unstable wave numbers according to Floquet analysis is far broader than the asymptotically observed range from DNS ($P=5$, $P=6$) implies there is a state-selection mechanism at work. The most likely mechanism is a difference in growth rates, as the observed states match perturbation wave numbers which are most unstable.

In order to help resolve this issue, further DNS investigations have been carried out for Re=4000. At each unstable wave number ($k=3$, 4, 5, 6, 7, and 8), the three-dimensional solution field is initialized with a combination of the axisymmetric base flow and the most unstable Floquet mode (at the corresponding phase of the base flow). The energy in the perturbation is set to be small enough that the initial growth of the instability is approximately exponential: the kinetic energy of the perturbation was chosen to be smaller than that of the base flow by a factor of 10^{-8}.

First, computations are carried out in an invariant subspace of the full geometry (see the discussion of Sec. III A). Once asymptotic states are reached in the subspace, the solution is projected to an unrestricted space (one with all Fourier modes), perturbed slightly in the $k=1$ mode with small-magnitude Gaussian noise, and left to further evolve. It is observed that if the invariant-subspace solutions are stable, energies in all modes $k \neq nP$ will die away asymptotically, otherwise another set of modes (those for a different P) will grow to replace the originally dominant set, which, after a transition period, dies away.

The outcomes of this investigation at Re=4000 were that solutions for $P=4$, 5, and 6 were stable (i.e., a new stable asymptotic state for $P=4$ was found, in addition to those already obtained at $P=5$ and 6), while the other states made the following transitions: $P=3\rightarrow 6$, $P=7\rightarrow 6$, $P=8\rightarrow 5$. Although $|\mu|$ for $k=7$, asymptotically unstable, is marginally larger than for $k=4$, stable, it appears that the selection of asymptotic states is indeed largely determined by the magnitude of the multiplier associated with the lowest-harmonic Floquet Fourier mode.

VII. STABILITY ANALYSIS OF TIME-AVERAGE FLOW

Having established that the observed asymptotic MRW states are closely associated with the most-amplified Floquet modes, it is natural to wonder how important the parametric excitation (T-periodicity) of the base flow is in creating the RW instabilities. To commence this investigation, we first examine the stability of the time-average axisymmetric M_0 flow, again at Re=4000—the time-average flow is illustrated in Figs. 3(e) and 4(c). While the time-average flow is not a solution of the Navier–Stokes equations, it may be an appro-

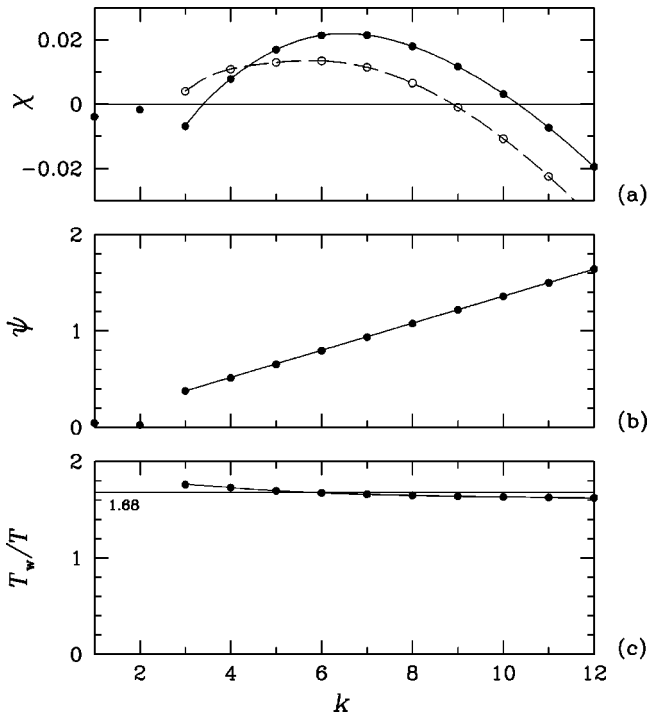

FIG. 12. Stability analysis of time-average flow at Re=4000. The real and imaginary parts χ and ψ of the leading eigenvalues are indicated as functions of wave number k by solid symbols and a line in (a) and (b), in (a), the open symbols and dashed line indicate the real part of the corresponding Floquet exponents. RW precession periods derived from ψ are shown in (c).

priate state to serve as the basis of an examination of RW instabilities, particularly if these are not tightly coupled to the time variation of the periodic M_0 states.

Eigenvalue information from the stability analysis is presented in Fig. 12. The real parts, χ, of the leading eigenvalues are shown as functions of wave number k in Fig. 12(a), where for purposes of comparison the real parts $\log(|\mu|)/T$ of the corresponding Floquet exponents, derived from the Re =4000 values of Fig. 7(a), are also represented. It can be seen that peak growth rates for the time-average flow are approximately double those for the periodic flow, and a slightly wider range of wave numbers is unstable. There is one major branch of solutions (for $k \geqslant 3$) which carries the unstable modes; the isolated modes at $k=1$ and $k=2$ are

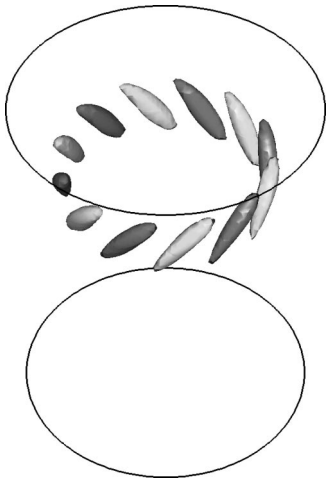

FIG. 14. Isosurfaces of vorticity magnitude for the most unstable mode ($k=6$) of the time-average flow at Re=4000. Isosurfaces are shaded according to the sign of the axial component of vorticity.

stable. The imaginary parts, ψ, of the leading eigenvalues, which indicate wave precession speed, are shown in Fig. 12(b), and it can be seen that to a very good approximation a linear relationship exists between precession speed and wave number for the unstable modes. Dimensionless RW periods are computed as $T_w/T = 2\pi k/\psi T$ and shown in Fig. 12(c): the predicted periods agree very well with the DNS observations (and also with values derived from Floquet analysis, cf. Fig. 9).

Mode shapes (eigenvectors) from the stability analysis of the time-average flow are presented as contours of kinetic energy for the unstable modes in Fig. 13. At the same wave numbers, the shapes of the unstable modes are quite similar to those for the Floquet modes seen in Fig. 10. A perspective view showing isosurfaces of vorticity magnitude for the most unstable mode, $k=6$, shown in Fig. 14 confirms the structural similarity to the equivalent Floquet mode (cf. Fig. 11).

VIII. STABILITY ANALYSIS OF STEADY FLOW

Now that we have seen that the unstable modes of the time-average axisymmetric flow bear a high degree of similarity with the equivalent Floquet modes, we turn to stability

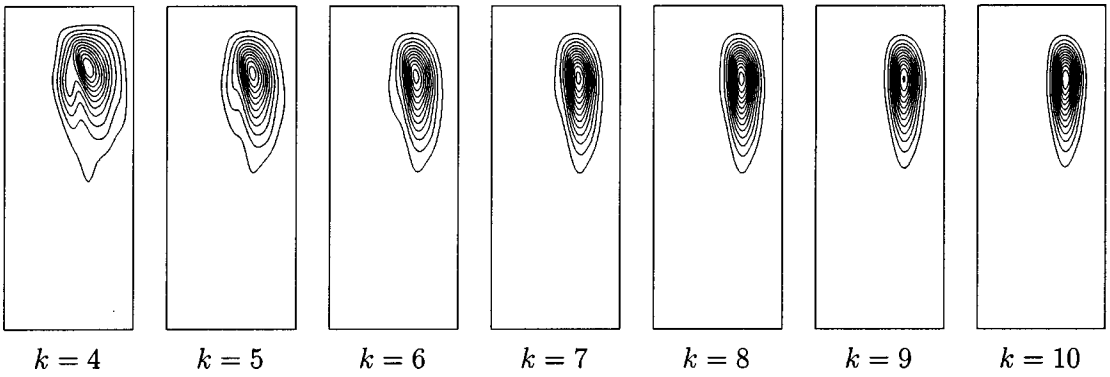

FIG. 13. Contours of kinetic energy in the meridional semiplane for unstable modes of the time-average flow at Re=4000 in wave numbers k as indicated. In each panel, cylinder axis is to the left-hand side, rotating end wall at bottom.

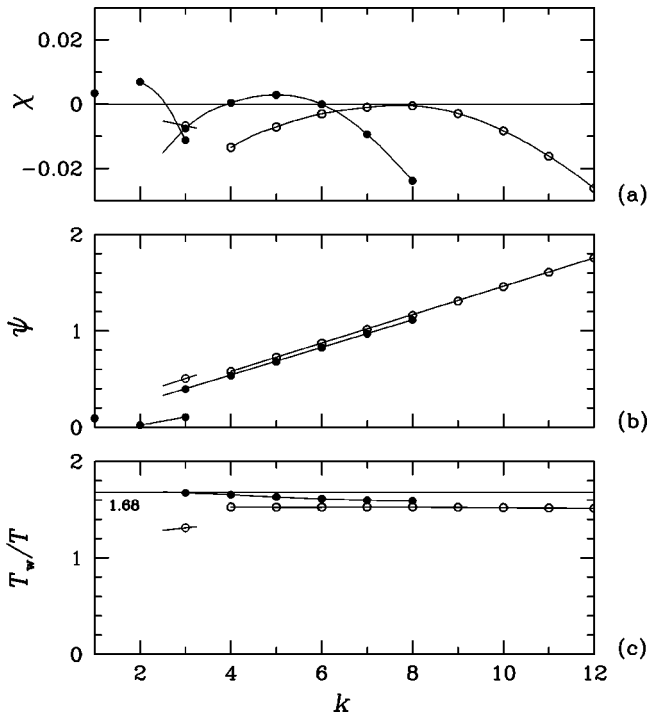

FIG. 15. Stability analysis of steady flow at Re=4000. Real, χ, and imaginary, ψ, parts of most unstable eigenvalues are shown as functions of wave number k in (a) and (b). RW precession periods derived from ψ are shown in (c). Solid and open symbols are used to denote different mode branches.

analysis of the steady flow at Re=4000. In contrast to the time-average flow, the steady flow *is* an exact, though unstable, solution to the Navier–Stokes equations. See Fig. 4(f) for the sectional streamlines of the steady flow; while the flow is generally similar to the time-average flow shown in Fig. 4(e), there are differences in detail, most prominently that the steady flow has a single axial vortex breakdown while the time average does not. The steady solution used as the basis of the stability analysis was obtained using the Newton method described in Sec. III C, initialized with the time-average flow.

Results derived from eigenvalues are shown in Fig. 15.

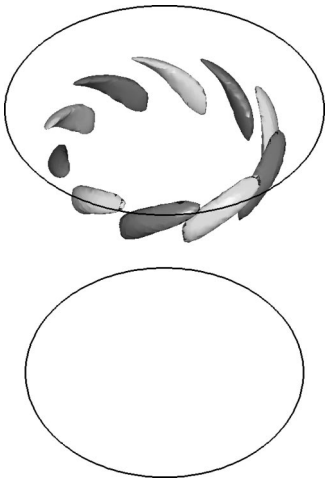

FIG. 17. Isosurfaces of vorticity magnitude for the most unstable mode ($k=5$) of the steady flow at Re=4000. Isosurfaces are shaded according to the sign of the axial component of vorticity.

It can be seen that there are a number of solution branches; it can be assumed from the good agreement with the observed RW periods [see Fig. 15(c)] that the solution branch that carries the three (marginally) unstable eigenvalues (for $k=4$, 5, and 6) corresponds to modes found in both the Floquet analysis and in the analysis for the time-average flow. This expectation is strengthened by the mode shapes revealed by the kinetic energy contours, Fig. 16, and by isosurfaces of perturbation vorticity magnitude, Fig. 17.

In addition to this main unstable solution branch it can be seen that also modes for $k=1$ and $k=2$ are unstable—the structure for these modes is quite different than that for the RWs previously observed. Energy for the $k=1$ mode is significant near the axis, and would lead to precession of axial vortex features.[8] A point of cross-reference is with the previous stability analysis of steady flows,[7] carried out for $k\leqslant 5$, which shows similar results: all studied wave numbers except for $k=3$ are predicted to be unstable to RWs at $\Lambda=2.5$, Re=4000.

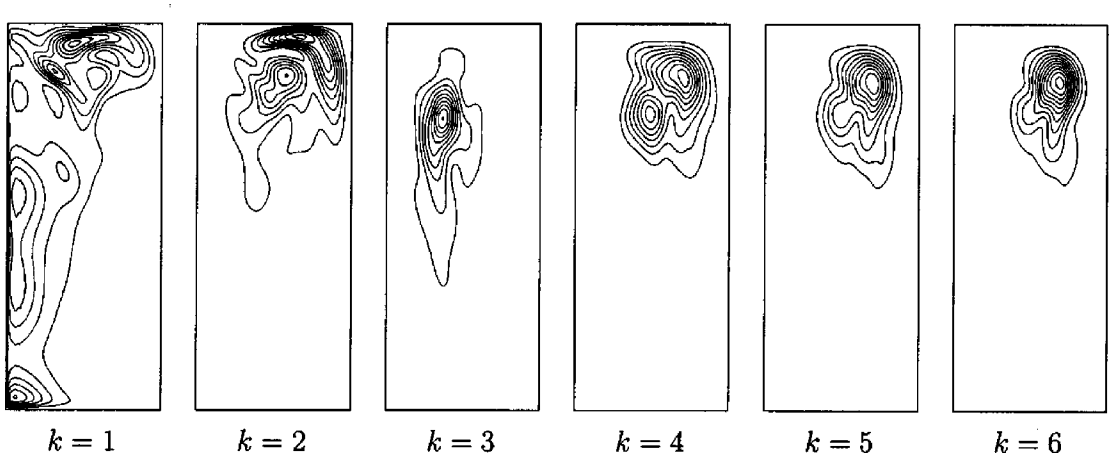

FIG. 16. Contours of kinetic energy in the meridional semiplane for leading modes of the steady flow at Re=4000 in wave numbers k as indicated. Leading mode for $k=3$ is stable, others are unstable.

IX. STABILITY ANALYSIS BASED ON VELOCITY PROFILES OF THE TIME-AVERAGE FLOW

Finally we turn to simple stability analyses based on velocity profiles of the time-average axisymmetric flow, as RW instabilities of this flow are closely linked to the MRWs of the periodic axisymmetric flow. Again, the analysis is carried out for Re=4000. The velocity profiles selected for this work were extracted on a radial traverse at $z/H=4/5$, at approximately the same elevation where energies in RWs are at their highest.

The profile of azimuthal velocity can be analyzed for centrifugal instability with the aid of Fig. 18. Rayleigh's criterion for axisymmetric centrifugal instability is that $\partial_r(r^2w^2)<0$, where w is the azimuthal component of velocity. With reference to Fig. 18(c), we observe that this quantity is indeed negative for $r\gtrsim 0.9R$, and is most negative near $r/R=0.95$. As Rayleigh's criterion is for axisymmetric centrifugal instabilities, it is not entirely appropriate to the task of predicting RW instabilities. But the fact that the radial location of a centrifugal instability indicated by this analysis is relatively remote from the observed RW locations ($r/R \sim 2/3$) helps to reinforce the conclusion, already suggested from the observed alignment of the RW structures, that centrifugal instability is not the primary cause of the RWs.

Another basis for analysis is suggested by the observation that the time-average azimuthal velocity profile in Fig. 18(a) is inflectional. While again the method is not entirely appropriate, we can analyze the stability of the velocity profile taken as a parallel shear flow. This means that wall-curvature effects, as well as streamwise changes in velocity profile, are taken to be unimportant. Fjørtoft's stability

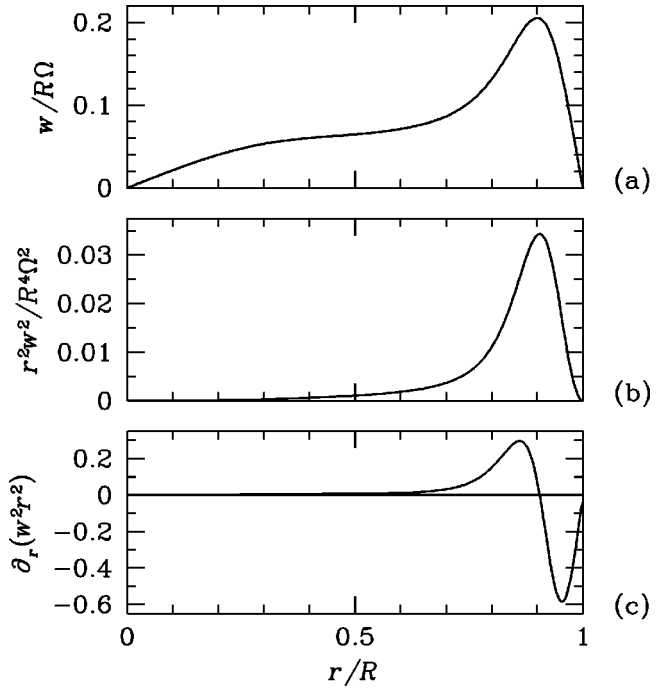

FIG. 18. Centrifugal stability analysis of axisymmetric time-average azimuthal velocity profiles for Re=4000. Profile data obtained on a radial traverse at $z/H=4/5$: (a) azimuthal, w, velocity profile; (b) profile of angular momentum r^2w^2; (c) first radial derivative of r^2w^2.

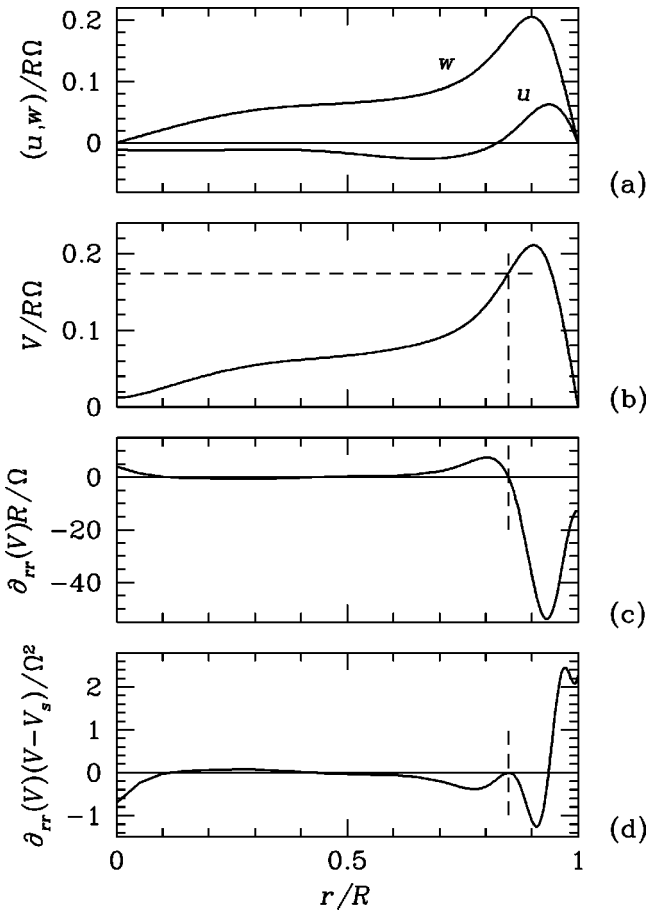

FIG. 19. Shear flow stability analysis of axisymmetric time-average velocity profiles for Re=4000. Profile data obtained on a radial traverse at $z/H=4/5$: (a) axial, u, and azimuthal, w, velocity profiles; (b) profile of $V=(u^2+w^2)^{1/2}$; (c) second radial derivative of V; (d) discriminant for Fjørtoft's stability criterion.

criterion[25] is that $\partial_{rr}V(V-V_s)\leqslant 0$ is a necessary condition for inviscid instability of parallel shear flows. Here V is a velocity magnitude and V_s is its value at a (radial) location where V is inflectional.

The axial, u, and azimuthal, w, velocity components of Fig. 19(a) are combined to form an approximate wall-parallel velocity magnitude $V=(u^2+w^2)^{1/2}$ profile in Fig. 19(b). Its second radial derivative is shown in Fig. 19(c), placing the inflection location at $r/R=0.84$. The discriminant for Fjørtoft's criterion is assembled and plotted in Fig. 19(d). It can be seen that $\partial_{rr}V(V-V_s)\leqslant 0$ over a wide radial range, $0.5\leqslant r/R\leqslant 0.95$. Despite the approximations in the application of the analytical technique, this result strongly suggests that RWs are primarily associated with an inviscid inflectional instability.

X. DISCUSSION AND CONCLUSIONS

Floquet stability analysis of axisymmetric periodic flows on the M_0 solution branch provides linearly unstable MRW perturbations which agree well with the asymptotic saturated states observed in DNS studies, both in terms of the location of the symmetry-breaking perturbations and in their predicted precession speeds. While MRW perturbations are un-

stable over a wider range of wave numbers than is occupied by the observed asymptotic states (for which the set of P-fold rotational symmetries is now $P=4$, 5, and 6 at $\Lambda=2.5$, $\mathrm{Re}=4000$), the observed states correspond well to the MRW instabilities at the most-amplified wave numbers. The orientation of the MRW vorticity (Fig. 11) strongly suggests that the instability is not primarily centrifugal in origin.

Stability analysis of the time-average flow shows that it too is unstable to RWs, and as the peak growth rates are higher than those for the MRWs found in the Floquet analysis, is more unstable than the original periodic flow from which it was derived. The fact that the RW instability occurs over a similar range of wave numbers, with similar mode shapes and precession rates as is found for the Floquet analysis, emphasizes the strong connection between the instabilities of the time-average and periodic flows—the parametric excitation of the periodic flow is not a primary contributing factor, although it does act to reduce peak growth rates and the wave number of the most-amplified perturbation.

Stability analysis of the corresponding steady flow again provides RWs that are unstable over a similar range of wave numbers as are observed asymptotically to be stable states in the DNS, but the connection with the Floquet analysis is much weaker than is the case for the time-average flow. A more diverse range of basic mode shapes is unstable than is the case for either the periodic or time-average flow. The set of unstable wave numbers agrees well with that of an earlier study of steady flows.[7]

The RWs most probably arise as a result of an inviscid inflectional instability of the swirling wall-jet velocity profile. Although the velocity profile would also support centrifugal instability near the cylinder wall, the radial locations of the inviscid inflectional instability is in better agreement with the observed MRW locations. In addition, as mentioned previously, the fact that the vorticity of the MRWs does not have streamwise alignment also suggests that centrifugal instability is not responsible for the instability. This is in contrast with results from another study,[26] where although the velocity profiles are both inflectional and centrifugally unstable, tight near-wall vortex structures align with the time-mean flow streamlines, suggesting centrifugal or crossflow instability is the primary cause of RWs in that case.

Vortex breakdown in itself does not appear to be directly significant in producing the RW instabilities. This can be said because the energy of the RW modes is almost always far removed from the axis (except for the $k=1$ mode of the steady flow in which will cause the vortex breakdown region to precess around the axis[8]), and because the time-average flow has no vortex breakdown.

This work has dealt primarily with stability analysis of the M solution branch. While flows of the V solution branch are also unstable to RWs over some of its Re extent, they are not amenable to Floquet analysis owing to the quasiperiodic nature of the axisymmetric solutions. It is possible that stability analysis of the time-average flows would yield useful information about the possible set of MRW states—thus far, only MRWs with fivefold rotational symmetry have been observed for the V branch.

The origin of the V solution branch itself is still an open question. In earlier work, it was conjectured that it results from mixtures of pairs of the first three axisymmetric modes to depart from the basic (axisymmetric, steady) state through Hopf bifurcations. Results presented here, in Sec. IV, suggest (but do not conclusively establish) another possibility: that it arises through an axisymmetric flip bifurcation instability of solutions of the M_0 branch. It is tempting to believe this relationship exists, at least in part on the basis of the frequency content of solutions of the V_0 branch—the two dominant periods are close to that of the M_0 branch, and its doubling.[13]

ACKNOWLEDGMENTS

The author gratefully acknowledges the assistance of D. Barkley and R. D. Henderson concerning analysis techniques and interpretation, and of J. M. Lopez through continuing discussions about this class of flows. The support of the Australian Partnership for Advanced Computing (APAC) through its Merit Allocation Scheme is also gratefully acknowledged.

[1] H. U. Vogel, "Experimentelle ergebnisse über die laminare Strömung in einem zylindrischen Gehäuse mit darin rotierender Scheibe," Technical Report No. 6, Max-Planck-Inst., 1968.
[2] M. P. Escudier, "Observations of the flow produced in a cylindrical container by a rotating end wall," Exp. Fluids **2**, 189 (1984).
[3] J. M. Lopez, "Axisymmetric vortex breakdown Part 1. Confined swirling flow," J. Fluid Mech. **221**, 533 (1990).
[4] J. M. Lopez and A. D. Perry, "Axisymmetric vortex breakdown. Part 3. Onset of periodic flow and chaotic advection," J. Fluid Mech. **234**, 449 (1992).
[5] D. Rand, "Dynamics and symmetry. Predictions for modulated waves in rotating flows," Arch. Ration. Mech. Anal. **79**, 1 (1982).
[6] E. Knobloch, "Bifurcations in rotating systems," in *Lectures in Solar and Planetary Dynamos*, edited by M. R. E. Proctor and A. D. Gilbert (Cambridge University Press, Cambridge, 1994), pp. 331–372.
[7] A. Yu. Gelfgat, P. Z. Bar-Yoseph, and A. Solan, "Three-dimensional instability of axisymmetric flow in a rotating lid–cylinder enclosure," J. Fluid Mech. **438**, 363 (2001).
[8] F. Marques and J. M. Lopez, "Precessing vortex breakdown mode in an enclosed cylinder flow," Phys. Fluids **13**, 1679 (2001).
[9] F. Marques, J. M. Lopez, and J. Shen, "Mode interactions in an enclosed swirling flow: A double Hopf bifurcation between azimuthal wave numbers 0 and 2," J. Fluid Mech. **455**, 263 (2002).
[10] J. L. Stevens, J. M. Lopez, and B. J. Cantwell, "Oscillatory flow states in an enclosed cylinder with a rotating end wall," J. Fluid Mech. **389**, 101 (1999).
[11] J. M. Lopez, F. Marques, and J. Sanchez, "Oscillatory modes in an enclosed swirling flow," J. Fluid Mech. **439**, 109 (2001).
[12] H. M. Blackburn and J. M. Lopez, "Symmetry breaking of the flow in a cylinder driven by a rotating end wall," Phys. Fluids **12**, 2698 (2000).
[13] H. M. Blackburn and J. M. Lopez, "Modulated rotating waves in an enclosed swirling flow," J. Fluid Mech. **465**, 33 (2002).
[14] G. Iooss and D. D. Joseph, *Elementary Stability and Bifurcation Theory*, 2nd ed. (Springer, Berlin, 1990).
[15] L. S. Tuckerman and D. Barkley, "Bifurcation analysis for timesteppers," in *Numerical Methods for Bifurcation Problems and Large-Scale Dynamical Systems*, edited by E. Doedel and L. S. Tuckerman (Springer, Berlin, 2000), pp. 453–566.
[16] G. E. Karniadakis, M. Israeli, and S. A. Orszag, "High-order splitting methods for the incompressible Navier–Stokes equations," J. Comput. Phys. **97**, 414 (1991).
[17] J. Guckenheimer and P. Holmes, *Nonlinear Oscillations, Dynamical Systems, and Bifurcations of Vector Fields*, 2nd printing (Springer, Berlin, 1986).
[18] L. S. Tuckerman, "Steady-state solving via Stokes preconditioning: Recursion relations for elliptic operators," in *11th International Conference*

on Numerical Methods in Fluid Dynamics, edited by D. L. Dwoyer, M. Y. Hussaini, and R. G. Voigt, Lecture Notes in Physics, Vol. 323 (Springer, Berlin, 1989), pp. 573–577.
[19]R. Barrett, M. Berry, T. Chan, J. Demmel, J. Donato, J. Dongarra, V. Eijkhout, R. Pozo, C. Romine, and H. van den Horst, *Templates for the Solutions of Linear Systems: Building Blocks for Iterative Methods* (SIAM, Philadelphia, 1993). Available through Netlib.
[20]Y. Saad, *Numerical Methods for Large Eigenvalue Problems* (Wiley, New York, 1992).
[21]D. Barkley and R. D. Henderson, ''Three-dimensional Floquet stability analysis of the wake of a circular cylinder,'' J. Fluid Mech. **322**, 215 (1996).
[22]S. A. Orszag, ''Fourier series on spheres,'' Mon. Weather Rev. **102**, 56 (1974).
[23]The presence of complex multipliers indicates that the MRWs arise from the periodic base flow via a Neimark–Sacker bifurcation (Ref. 14).
[24]H. L. Reed and W. S. Saric, ''Stability of three-dimensional boundary layers,'' Annu. Rev. Fluid Mech. **21**, 235 (1989).
[25]P. G. Drazin and W. H. Reid, *Hydrodynamic Stability* (Cambridge University Press, Cambridge, 1981).
[26]H. M. Blackburn, ''Sidewall boundary layer instabilities in enclosed swirling flow,'' J. Turbulence **2**, 9 (2001).